Underwater acoustic energy fluctuations during strong internal wave activity using a three-dimensional parabolic equation model

Georges A. Dossot, Kevin B. Smith, Mohsen Badiey, et al.

Citation: The Journal of the Acoustical Society of America **146**, 1875 (2019); doi: 10.1121/1.5125260
View online: https://doi.org/10.1121/1.5125260
View Table of Contents: https://asa.scitation.org/toc/jas/146/3
Published by the Acoustical Society of America

Underwater acoustic energy fluctuations during strong internal wave activity using a three-dimensional parabolic equation model

Georges A. Dossot,[1,a)] Kevin B. Smith,[2] Mohsen Badiey,[3] James H. Miller,[1] and Gopu R. Potty[1]

[1]*Department of Ocean Engineering, University of Rhode Island, Narragansett, Rhode Island 02882, USA*
[2]*Department of Physics, Naval Postgraduate School, Monterey, California 93943, USA*
[3]*College of Marine and Earth Studies, University of Delaware, Newark, Delaware 19716, USA*

(Received 4 January 2019; revised 5 August 2019; accepted 19 August 2019; published online 1 October 2019)

The three-dimensional Monterey–Miami parabolic equation model is used to simulate a nonlinear internal wave (NIW) crossing the sound field in a shallow water environment. The impetus for this research stems from acoustic measurements taken during the Shallow Water '06 (SW06) field experiment, where a NIW traversed the water column such that soliton wavecrests were nearly parallel to the source–receiver path. Horizontal refraction effects are important in this scenario. A sound speed profile adapted from experimental SW06 data is used to simulate the NIW, assuming variations along the wavecrests (e.g., curvature) are negligible. Broadband and modal energy metrics show acoustic fluctuations due to internal wave activity. Repeated model runs simulate the NIW crossing the parabolic equation (PE) field over space and time. Statistical analysis shows the PE data are best fit by a lognormal distribution but tends to an exponential distribution during certain scenarios. Small angle differences between the acoustic track and the propagating NIW cause substantial differences in energy distribution throughout the PE field. While refraction effects due to the leading edge of the NIW's arrival are important in all cases, the impacts of focusing and defocusing in the perfectly parallel case dominate the field fluctuations. In the non-parallel case, the strong fluctuations introduced by the passage of the NIW are of similar order to the refraction off the leading edge. https://doi.org/10.1121/1.5125260

[JFL] Pages: 1875–1887

I. INTRODUCTION

Strong nonlinear internal waves (NIWs) are well-known to occur in shallow water, usually near the continental shelf break, due to interactions with tidal forcing and the non-uniform ocean bathymetry. Since the early 1990s, it has been clear that these NIWs can have a profound effect upon acoustic propagation, and further investigating this phenomenon was a primary motivation for the Shallow Water '06 experiment (SW06).[1] The purpose of this article is to highlight a specific data set from the SW06 experiment, which shows evidence of horizontal refraction of acoustic signals due to a passing NIW. To provide insight into the acoustic data, a measured oceanographic sound speed profile was employed as the primary environmental input to a three-dimensional (3-D) parabolic equation model. Broadband model results show that small angle deviations (within $\pm 5°$) between the source–receiver and the NIW front cause substantial differences in the fluctuating sound field.

An experiment in the Yellow Sea is often referred to as the starting point for investigations in this area, where it was found that internal waves were responsible for "anomalous" acoustic fluctuations, that have since become hallmark features of NIW activity. By using parabolic equation (PE) simulations and normal mode decomposition, mode-coupling was the suggested dominant physical mechanism responsible for changes in measured signals propagating through NIW packets.[2] Following this, a theoretical study implementing the parabolic approximation in the horizontal plane with vertical modes along the depth dimension treated horizontal refraction due to NIW activity, introducing *focusing* and *defocusing* effects when the acoustic path is parallel to soliton fronts.[3] Shortly thereafter, fully 3-D PE techniques were used to simulate the time evolving NIW field, ascertain azimuthal dependence, and examine 3-D propagation effects.[4–11] More recently, PE models have been used to analyze increasingly complex scenarios that are especially relevant to circumstances when the source–receiver path is nearly parallel to the NIW wavecrests, and where horizontal refraction dominates.[12–16]

Large scale ocean acoustic experiments, including PRIMER,[17] SWARM,[18,19] ASIAEX,[20,21] and SW06 have produced field data that have significantly improved our understanding of NIW phenomena and their relative importance to the sound field. Previous experiments and reports have identified acoustic intensity fluctuations varying between 3 and 20 dB due to interactions with the acoustic field and NIWs. Specifically, Badiey *et al.*[22] identified acoustic propagation regimes based upon angle dependence of an internal wave front relative to the source–receiver path. When the source–receiver path is nearly perpendicular to a NIW, mode coupling dominates. At angles closer to 45°, adiabatic propagation dominates because neither mode

[a)]Also at: The Naval Undersea Warfare Center, 1176 Howell Street, Newport, RI 02841, USA. Electronic mail: georges.dossot@navy.mil

coupling nor horizontal refraction effects play a strong role. Finally, at low angles, horizontal refraction and focusing dominate. Theoretical predictions of horizontal refraction effects were previously offered by Katsnelson and Pereselkov.[3] Shortly thereafter, Badiey *et al.*[6] documented horizontal regime fluctuations between 6 and 7 dB derived from SWARM-95 (Ref. 16) data, and fluctuations of 7 dB in SW06 data have been recognized by Luo *et al.*[23]

Figure 1 depicts our situation of interest, where a propagating NIW is parallel to the source–receiver path. Horizontally refracted modal rays for an acoustic source at different locations relative to the NIW are shown. This situation can be interpreted as an acoustic source being towed through the NIW, or alternatively (and similar to the data presented in this paper), a NIW propagating past a stationary acoustic source. Sound speed differences in the horizontal plane due to NIW activity will influence the path traveled by each modal ray. Because the total acoustic field will be the summation of all trapped modes in the water column, and each mode travels an individual path, multipath constructive and destructive interference will occur.

As the NIW passes through the sound field, time-varying acoustic fluctuations become apparent, and regimes can be defined based upon the position of the NIW relative to the acoustic track. These regimes separate the dominant physical processes versus time, and are labeled the *quiescent* regime, the *refraction* regime, and the *NIW interference* regime—the latter being a combination of focusing and defocusing effects. Note that Fig. 1 delineates these regimes at different depths in the water column for clarity only—the modal rays are not depth dependent. At first (zero time or zero range), the approaching internal wave will have little to no impact upon the acoustic field, simply because it is too far away. This can be termed the *quiescent*[8] regime, where any fluctuations are due to stochastic scattering or a mildly fluctuating water column. As the NIW's leading edge approaches the source, modal rays will refract off the first soliton. This *refraction* regime will create an interference pattern in the horizontal plane akin to a Lloyd's mirror phenomenon.[12,15,24] At the moment the leading soliton centers itself over the acoustic source, defocusing spreads the sound outwards in an "anti-duct" fashion. Then, as the wave progresses and solitons trap the acoustic source, focusing occurs in a horizontal "duct." Combined, both defocusing and focusing effects due to several solitons in the NIW train create a complicated and strong *interference* regime. As the NIW fully propagates and only vestiges of the soliton train are left, fluctuations will taper off.

The spatiotemporal horizontal refraction effects summarized above are considered well established. This paper investigates the particular case where the difference between the source–receiver path and the propagating NIW front falls within $\pm 5^{\circ}$. We show that small angle deviations cause measurable differences in the fluctuating sound field. The data highlighted in this article demonstrate intensity fluctuations from an internal wave event experienced aboard the University of Delaware's research vessel (R/V) Sharp during the SW06 experiment. The 3-D MMPE model, which had been previously used to examine the impact of NIWs upon shallow water acoustics,[25] was employed to better understand the SW06 data of interest.

Our paper is organized in the following manner: We provide an overview of the SW06 experimental setup and focus on the data set of interest, using intensity metrics as a way to characterize acoustic fluctuations. Modal decomposition provides further insight into the fluctuating sound field. We discuss considerations relevant to the PE model for our particular case. Following this, we simulate the NIW propagating over time and space by executing repeated model runs. A statistical analysis of all modeled data serves as a reference point across example scenarios. The model shows the dependency of small angle deviations between the source–receiver track and the NIW front.

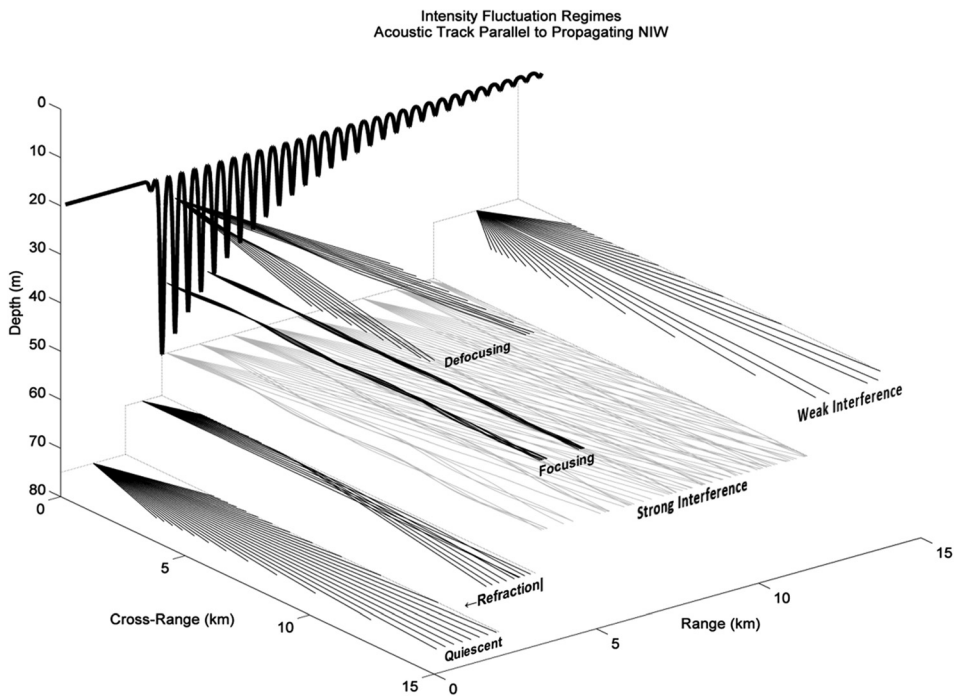

FIG. 1. Time varying intensity fluctuation regimes for a propagating NIW field passing an acoustic source. An acoustic source emits horizontally refracted modal rays at frequency f and mode number M. Note: Rays are not depth-dependent, and are plotted at different levels to clarify different regimes. A quiescent regime is followed by a refraction regime prior to the NIW's arrival. As the NIW passes over an acoustic source both focusing and defocusing cause a complicated interference regime.

II. EXPERIMENTAL SETUP AND COLLECTED DATA

A. Acoustic setup and internal wave event

The SW06 experiment took place during the summer of 2006 off the coast of New Jersey with a primary goal of further understanding acoustic propagation in coastal waters. The multi-institutional endeavor was sponsored by the Office of Naval Research, and included numerous research vessels, scientific moorings, and principal investigators. The experimental location was proximate to the continental shelf break front, near the site of previous acoustic studies,[18] and was ideally situated in an environment where internal waves are known to occur. During SW06, the R/V Sharp was deployed for a three-week period (1–21 Aug.) and observed 58 internal wave events.

Figure 2 depicts the portion of SW06 experimental area relevant to internal wave *Event 44*, the 44th event witnessed by the R/V Sharp. The maps in this figure show the primary acoustic receiver, environmental moorings, and the R/V Sharp's deployed J-15 source. During periods when the moored SW06 sources were not transmitting, the R/V Sharp transmitted a series of repeating signals every 3 min, including 23 broadband chirps (50–450 Hz) at 74 m depth. The water depth was 80 m. The R/V Sharp was located 15 km from the Woods Hole Oceanographic Institution (WHOI) *Shark* 16-element vertical line array (VLA), such that the acoustic path was parallel to expected NIW soliton fronts. At roughly 3:30 a.m. [Greenwich mean time (GMT)] on August 14th, the surface expression of a large slow-moving internal wave train appeared on the ship's radar. Overlaid on the maps are snapshots of radar imagery as Event 44 approached, arrived at, and moved past the ship and acoustic source.

Approximations from the radar imagery show that the leading edge of the soliton train propagated at roughly 0.5 m/s, with little evidence of curvature (although often known to occur). Radar also showed the NIW train propagated northwest by west at a bearing of 308 deg for 5 h, evident between 4:00 and 9:00 GMT. Environmental water column measurements confirm a strong internal wave event during this time. The bottom panels of Fig. 3 exhibit internal wave activity at the R/V Sharp's J-15 source, at the WHOI VLA receiver, and at an environmental mooring midway between the source and receiver. The R/V Sharp's downward looking acoustic Doppler current profiler (ADCP) recorded evidence of a strongly oscillating pycnocline as the internal wave passed beneath the ship. Environmental mooring SW32, located between the source and receiver, also shows very strong internal wave activity at a midway point between transmission and reception. Finally, interpolated sound-speed values at the WHOI VLA exhibit internal wave activity during the same time period. Comparing internal wave activity at the source and receiver, the environmental data indicates the NIW arrived at the receiver location about 1 h prior to the acoustic source location. Assuming a speed of 0.5 m/s (estimated by radar imagery) we approximate a bearing difference of approximately 5 deg between the propagating internal wave front and the source–receiver path. This geometry results in a 15-km-long source–receiver path, with a nearly parallel, slow-moving, and straight-line internal wave front reaching the acoustic receiver roughly 1.5 km before the acoustic source. Given these environmental and experimental conditions, we conclude that horizontal refraction effects dominate acoustic fluctuations during the approach and passage of the NIW.

B. Broadband data analysis

In order to quantify the intensity fluctuations that occurred during NIW activity, we employ methods described by Duda *et al.*[26] and Fredericks *et al.*,[27] which have previously been used to treat acoustic data from the PRIMER and ASIAEX experiments. In these analyses, acoustic data spanning several days were quantified by decomposing intensity and energy values into tidal and subtidal frequencies, thereby evaluating the impact of ocean processes in an all-inclusive convention. Here, we use the same metrics to analyze a discrete NIW event, correlating it with local oceanographic processes to better understand the variability of the acoustic field during a much shorter timescale.

Temporally integrated energy, I_τ, of each signal k, and at depth z, was chosen as the primary tool to correlate

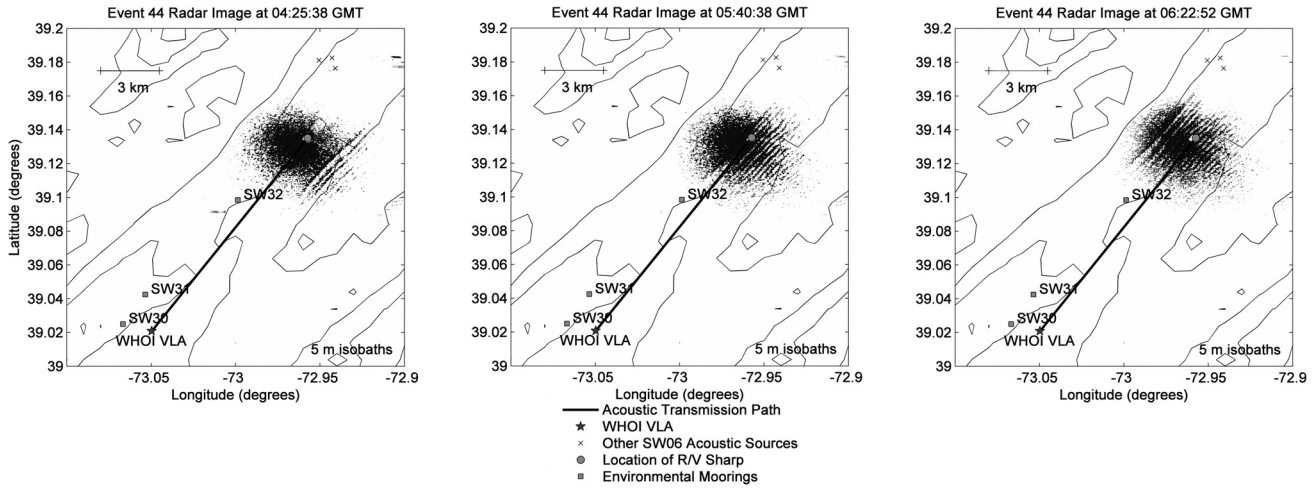

FIG. 2. A strong internal wave event propagated nearly parallel to the source–receiver acoustic track (R/V Sharp J-15 and WHOI VLA, respectively). Ship radar detected the surface expression of the NIW as it approached, passed beneath, and left the R/V Sharp.

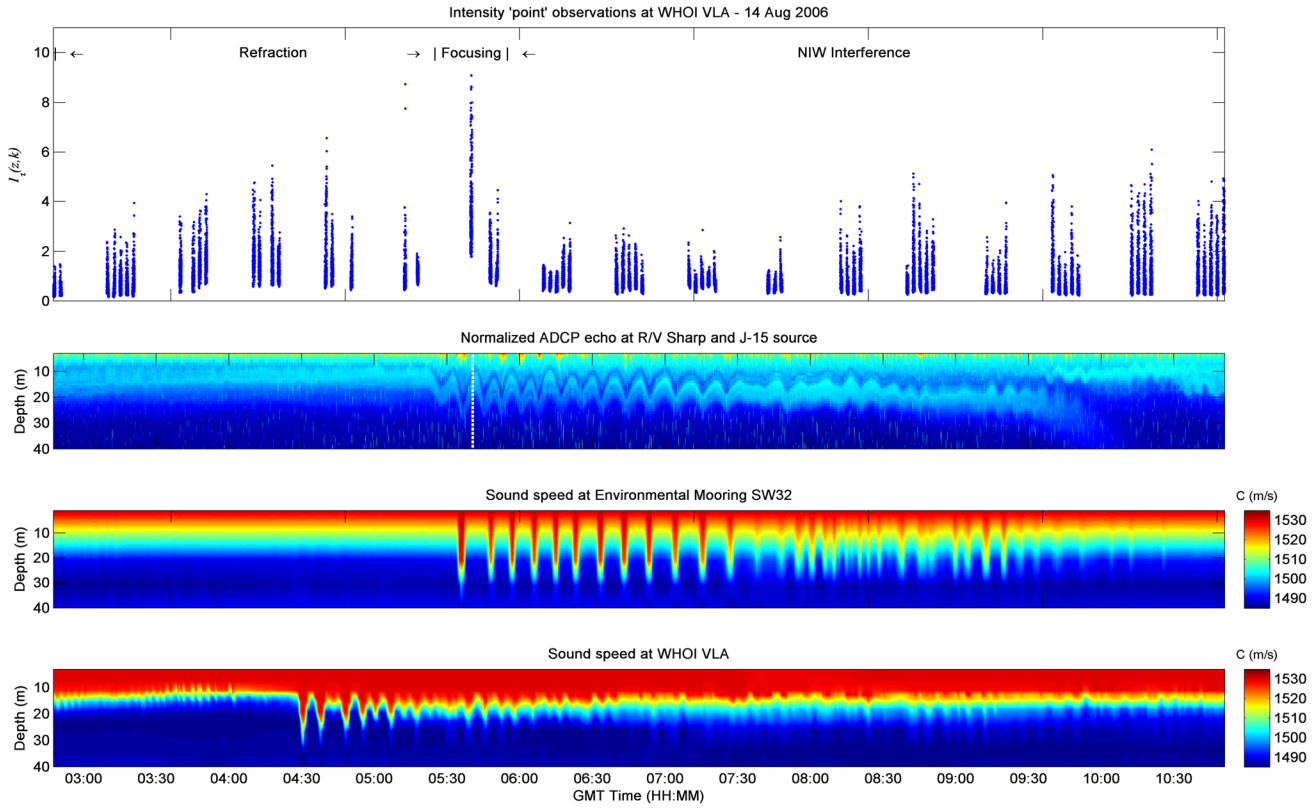

FIG. 3. (Color online) Acoustic data compared to environmental data. (Top) Measured normalized energy levels received upon each hydrophone of the WHOI VLA versus time. Refraction occurs prior to the NIW's arrival, with possible focusing as the NIW arrives at the acoustic source. A complicated NIW interference regime follows; (bottom three plots) Environmental sensors including R/V Sharp ADCP (at the acoustic source) showing NIW pycnocline, mooring SW32 (midway between source–receiver), and interpolated sound speed at the WHOI receiving VLA, all exhibiting strong internal wave activity.

acoustic data to oceanographic evidence of NIW activity because this metric provides insight into the depth dependence of acoustic energy, and also helps to discriminate time varying energy changes over the water column. Prior to performing metrics upon the chirp signals, receptions were high-pass filtered (100 Hz cutoff frequency) to remove broadband noise, and match-filtered to extract the transmitted chirp signal. $I_\tau(z,k)$ is calculated [via Eq. (1)] by integrating the match- and high-pass filtered intensity I, over the energetic duration of the signal τ (~ 0.4 s), with these time limits carefully chosen in order to reduce residual noise contributions, but to also incorporate multipath arrivals. The I_τ metric provides visual interpretation of the peak energy variability, and variability of energy distribution throughout the water column. These data are then normalized such that their arithmetic mean value is one; $I_\tau = 1$. Normalizing data in this manner offers good visualization of fluctuating signal intensifications ($I_\tau > 1$); however interpreting signal fades can be more difficult to discern because all values below the mean are bounded by $0 < I_\tau < 1$:

$$I_\tau(z,k) = \int I(\tau,z,k)\,d\tau. \tag{1}$$

All signals were inspected such that chirp arrivals overshadowed by noise were discarded.

The top panel of Fig. 3 shows temporally integrated energy receptions during Event 44 on a linear scale for all hydrophones of the WHOI VLA. We refer to these individual receptions as "point" measurements[27] throughout this paper. For direct comparison, these data are plotted against the same timescale as the oceanographic information previously discussed. Environmental measurements confirm internal wave activity along the entire acoustic track. Again, breaks in acoustic data are due to temporary pauses in the R/V's transmissions during other SW06 source activity.

Figure 4(a) shows a normalized histogram of these data, with a total number of $N = 16\,100$ samples. Overlaid is a fitted lognormal probability density function (PDF) yielding a lognormal mean, $\hat{\mu}$, of 0.986, and a lognormal variance, $\hat{\sigma}^2$, of 0.417. We see that the entire data set is well-fitted by this type of distribution, which agrees with previous observations given by Fredericks *et al.*[27] for acoustic data influenced by NIW activities (high-frequency oceanographic processes). It is important to note that the highest energy points that are visually apparent in Fig. 3 are, in fact, outliers and highlight fluctuations that are well above the mean. For this reason, interpreting PDFs which represent portions of these data are a more appropriate way to infer the general impact of physical processes on the acoustic field.

The entire data set serves as a comparison point for breaking the data into the proposed refraction, focusing, and NIW interference regimes. Based upon the oceanographic data, the data sets are broken into expected periods of refraction, focusing, and NIW interference (labeled in the top panel of Fig. 3). Figure 4(c) shows the lognormal PDFs for these data separated into each regime to show differences or

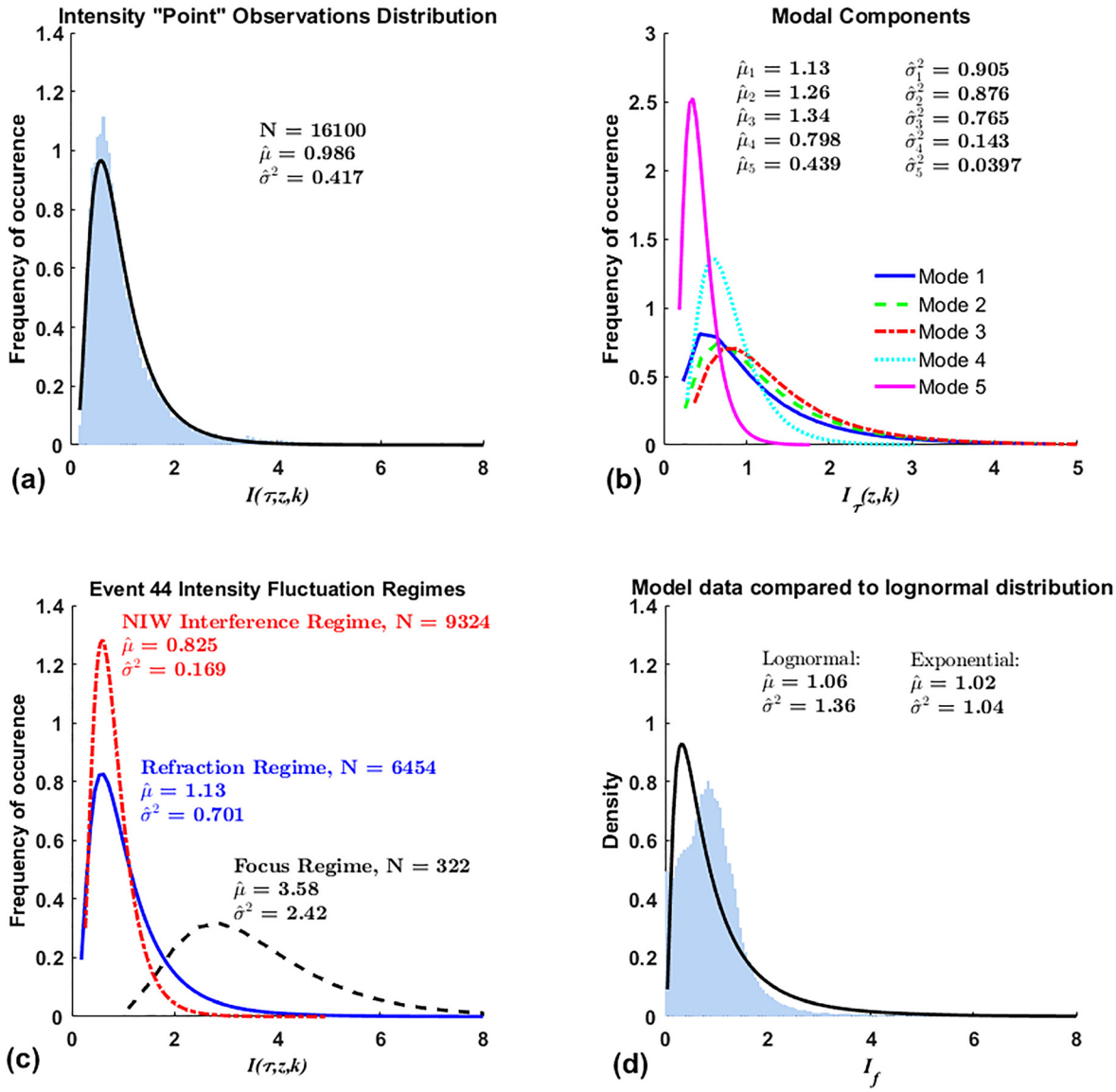

FIG. 4. (Color online) Energy distributions for (a) measured data during Event 44, (b) the modal components, (c) subsets of data corresponding to time periods as the NIW crosses the acoustic path, and (d) modeled data for a simulated NIW crossing the acoustic path.

similarities between these areas of acoustic data. The acoustic focusing between solitons dominate both signal intensification and signal variability, while refraction effects prior to the NIW's arrival cause similar variability as NIW interference effects.

C. Modal decomposition

Broadband modal beamforming was carried out according to the methods described by Crocker *et al.*,[28] such that the signals were match-filtered and weighted by their modal components in the frequency domain. A spectrogram of a non-match-filtered LFM chirp signal received upon the eighth hydrophone of the WHOI VLA (39 m deep) is displayed in the far-left panel of Fig. 5. This example signal spectrogram was recorded at the start of the acoustic data set during Event 44; it was band-pass filtered between 70 and 325 Hz in order to remove low frequency noise, and also to remove a 330 Hz tone (instrument noise) that was persistent throughout these data. The spectrogram shows a splitting at the "foot" of the chirp (below 150 Hz) which indicates separate modal arrivals, and modal dispersion in the acoustic waveguide.

Modal decomposition of this signal is displayed in the right-most panels of Fig. 5 for the first five modes, serving to explain some of the frequency dependent variability. For consistency across plots, the color scale for each modal arrival is normalized and identical. Specific to this particular sample, Mode 1 carries energy in the lowest part of the frequency spectrum (less than 200 Hz), whereas Mode 5 carries energy in the upper part of the spectrum (greater than 200 Hz). Modes 2, 3, and 4 carry energy throughout the entire 70–325 Hz band. The modal decomposition shows splitting at the foot of the chirp can be attributed to separate mode arrivals.

Figure 4(b) shows the modal energy distributions for the duration of Event 44. The lognormal mean and variance for each modal distribution is also annotated. Similar to the approach employed in calculating I_τ, these signals have been match-filtered, and the energy for each modal component

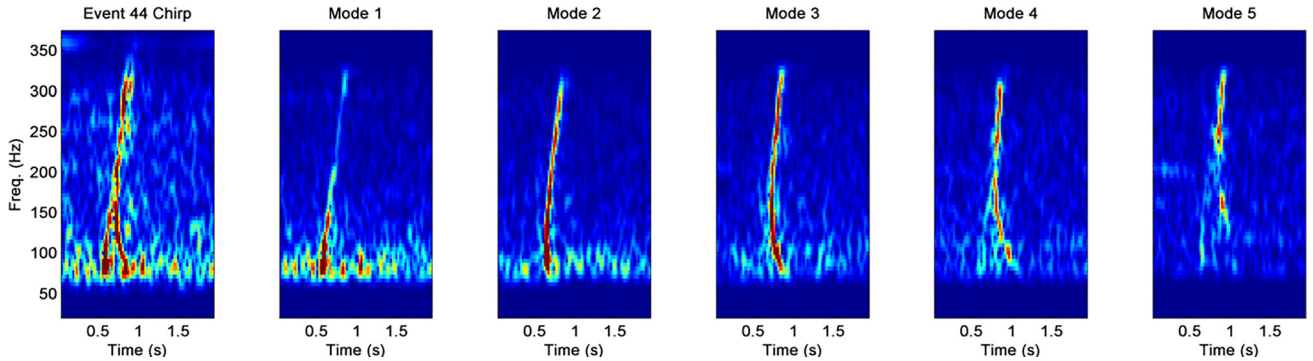

FIG. 5. (Color online) Spectrogram showing a received chirp signal upon the eighth hydrophone (at 39 m deep) of the WHOI VLA (left). This signal is broken down into broadband modal components for modes 1–5 (right panels). Note the "splitting" of the signal can be explained by separate modal arrivals. Color scales across plots are identical.

was calculated by integrating under the energetic region of the received mode arrival. Modes 1–3 dominate energy delivery and signal variability upon the VLA, while modes 5–6 carry less energy and variability.

To further examine the fluctuating sound field just prior to and at the NIW's arrival, stacked time arrival plots for each mode are shown in Fig. 6. The arrivals are divided into groupings, where Groups 1–4 show modal arrivals before the onset of the NIW, and Group 5 shows where NIW activity starts to cross into the source–receiver path. Modes 1–4 show steady arrivals until the NIW crosses the source–receiver path and then arrivals become highly variable. Mode 5 energy increases as the NIW approaches, and the arrivals become unresolvable once the NIW crosses the source–receiver path.

III. THREE-DIMENSIONAL PARABOLIC EQUATION MODEL

To better understand the impact of Event 44 on the sound field, we implement an acoustic model. The primary tool used in this analysis was the MMPE model, an outgrowth of the University of Miami parabolic equation model (UMPE),[29] chosen for its ability to predict horizontal refraction effects in a 3-D shallow-water environment.

The version used in this study utilizes the Cartesian coordinate system such that *range* is represented along the *x*-axis, *cross-range* along the *y*-axis, and *depth* along the *z*-axis. The model permits implementation of a fully 3-D sound speed profile, and therefore allows for insertion of the NIW as the primary environmental water-column variable to induce

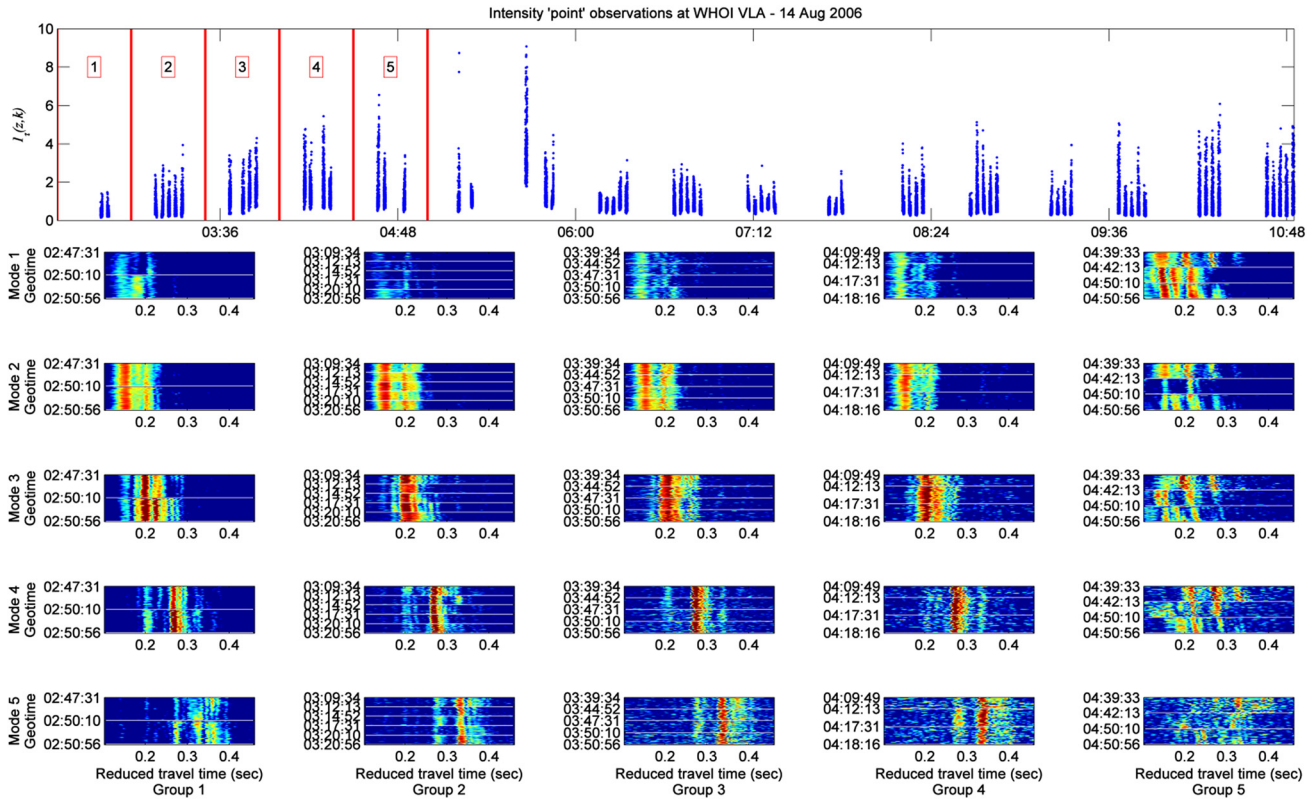

FIG. 6. (Color online) Stacked time arrival plots for sections of Event 44 data where horizontal refraction may be occurring. Top panel shows measured normalized energy levels received upon each hydrophone of the WHOI VLA versus time. Segments of data are divided into five groupings. The first five modes for each grouping are plotted column-wise in the bottom panels.

perturbations into the acoustic field. The model also fully accounts for cross-range variation, or "horizontal coupling," along the y dimension. Retaining this y-dependence is similar to retaining azimuthal dependence in the cylindrical derivation, rather than assuming an uncoupled azimuthal approximation (UNCA).[30] For our problem at hand, this dependence is important, so that we adequately capture refractive effects due to NIW activity. Since we are interested in 3-D refraction effects, we desire the maximum amount of energy possible to be distributed in the lateral (cross-range) dimension. The model implements a wide-angle source function based on the Thomson and Bohun field starter.[31]

A. Broadband frequency considerations

During the acoustic analysis of measured experimental data, acoustic energy I_τ [Eq. (1)] served as our primary metric to evaluate fluctuations induced by NIW activity. To directly compare modeled versus measured data, one would need to sufficiently model the signal in frequency and approximate the time arrival via an inverse Fourier transform. This approach becomes challenging from a computational resource perspective. Instead, we offer an approximation of received energy by applying Parseval's theorem. Let our received signal be represented in the time domain by $P(t)$ and in the frequency domain by $p(f)$, such that

$$\int_\tau |P(t)|^2 dt = \int_{BW} |p(f)|^2 df. \tag{2}$$

Since energy is conserved in both the time and frequency domains, instead of an integral over time (I_τ), we perform the calculation over frequency and denote it by I_f. Therefore, the approximate energy of the acoustic signal based on several frequency samples can be written as

$$I_f = \int_{BW} |p(f)|^2 df \approx \frac{BW}{N} \sum_{i=1}^{N} |p(f_i)|^2, \tag{3}$$

where BW represents the bandwidth of the signal, modeled at N discrete samples. For this study we limited the modeled signal bandwidth to 100–300 Hz, evaluated at $N = 17$ (12.5 Hz sampling). Our calculation of I_f requires a summation at a fixed point in space and across N frequencies; therefore we require the spatial grid to be fixed across our source bandwidth. Additionally, choosing an appropriate spatial sampling grid became an important factor when choosing the modeled signal's bandwidth. A spatial grid corresponding to 175 Hz allowed for acceptable sampling over a 100–300 Hz bandwidth and was chosen as the final configuration for our investigation.

B. Bottom considerations

Because sea bottom properties have profound impacts upon the amount of acoustic energy that remains trapped in the water column, a sensitivity analysis of bottom parameters upon the I_f metric was performed. Previous estimates from geoacoustic inversions by Jiang *et al.*[32] and Potty *et al.*[33] provided bounds for the geoacoustic parameters, shown in Table I. By varying these 11 parameters between realistic maximum and minimum values, 2048 iterative two-dimensional (2-D) model realizations were accomplished. The sensitivity analysis concluded that layer-one compressional attenuation to be the most influential factor, followed by layer-one compressional speed dependence, and then by layer-one shear speed dependence. The model treats shear by employing an equivalent fluid approximation given by Zhang and Tindle,[34] where the layered solid is replaced by a fluid with adjusted parameters. Parameter values centered across the range of possibilities were chosen as the final input parameters to the model (Table I). Regarding bathymetry, because we are primarily concerned with water-column induced acoustic perturbations, we only consider a flat bottom with a constant depth of 80 m. This simplification is relatively true of the SW06 experimental area, which varied no more than ±2.5 m over the Event 44 acoustic track.

TABLE I. Layer 1 geoacoustic parameters.

Parameter	Layer 1	Layer 2
Density, ρ_1 (kg/m^3)	2.09	2.361
Compressional speed, c_{p1} (m/s)	1683.75	2164.5
Compressional attenuation, α_{p1} (dB/m/kHz)	0.172	0.378
Shear speed, c_{s1} (m/s)	161.45	825.2
Shear attenuation, α_{p1} (dB/m/kHz)	0.754	0.857
Layer height, H_1 (m)	22.65	N/A

C. Internal wave sound speed profile

Based upon measurements captured by the environmental sensors, we can safely assume the NIW covered the entire 15 km acoustic track. Radar showed there was little (or no) curvature to the wavefront, and that the first soliton arrived at the receiving VLA roughly 1 h before reaching the J-15 source. We have reasonable knowledge of NIW activity at the source, the receiver, and a midway point at environmental mooring SW32. Because of incomplete knowledge of the internal wave's structure over time and space, we assume that the time series captured by the environmental sensors represent a valid approximation of the NIW's structure in space. This assumption infers that the wave evolution is frozen as it traverses the acoustic track; and that it does not significantly undulate over this period of time. Based upon our interpretation of the marine radar, we assume that the NIW can be modeled in a straight-line fashion. In other words, the solitons (and especially the leading edge) contain no curvature. NIW curvature has been shown to be acoustically important when it exists.[14–16] For simplicity, we assume that the NIW does not vary in range. Therefore, the internal wave activity captured at environmental mooring 32 (situated midway between the source and receiver) adequately represents the NIW's structure over the entire 15 km acoustic track.

IV. IMPACTS OF NIW ACTIVITY UPON THE SOUND FIELD

A. Narrowband time-dependent NIW propagation

The sound speed profile of the passing internal wave captured on environmental mooring 32 served as the primary

environmental input for the 3-D propagation model. Mm. 1 simulates Event 44 traversing a 300 Hz sound field by concatenating repeated model runs together. The top left panel shows the time-varying sound speed profile, which remains constant versus range (x axis). The second panel shows depth integrated intensity as the NIW propagates through the modeled ocean volume over time and space. The evolution of the sound field clearly shows examples of *refraction* (prior to the NIW's arrival), *defocusing* (arrival at the acoustic source), and *focusing* (trapping of the acoustic source between solitons). While these specific scenarios are considered well established phenomenon that are known to introduce energy fluctuations into the sound field, the model also shows more complex interference patterns, such as secondary ducting and refraction of energy between solitons. The simulation highlights how NIW activity creates significant modulations in the acoustic field over short ranges (or timescales). To better understand the subtleties associated with NIW modulations, a modal analysis is helpful.

Mm. 1. Depth integrated intensity and modal decomposition of the PE field for modes 1–5 for a 300 Hz source. The simulated internal wave traverses the sound field, creating refraction, focusing, and defocusing effects. This is a file of type "mp4" (14.7 MB).

Mm. 1 also shows the first five modes of the modeled ocean volume. Our approach to modal analysis was to decompose the full PE field as a post-processing task, rather than initialize the PE field with a modal starter. The expected eigenfunctions for the acoustic field were calculated by the KRAKEN normal mode program[35] using identical PE sound-speed profiles and bottom parameters. The PE field was then decomposed into normal modes by applying the sample mode shape approach.[36] It should be noted that the wide angle PE field does not exactly decouple into the Helmholtz equation's normal mode basis set.[37] Anomalies from the normal mode decomposition of the PE are not evident in the examples provided, but would be apparent as banding effects in higher order modes.[38]

Prior to the NIW's arrival at the acoustic source, we see that mode 1 was not heavily excited; this is due to the source's deployment depth. However, as sound propagates through the soliton train, mode coupling from the higher order modes transfers energy into mode 1. This transfer is especially remarkable at angles approaching an acoustic path perpendicular to the NIW front, which corroborates well with previously published results.[22,39,40] Above mode 2, we see increased initial modal excitement, and looking across panels we notice that horizontal refraction effects generally increase as mode number increases. As the leading soliton arrives at the acoustic source, defocusing causes a shadow-zone which is more prominent in the higher order modes. This indicates that a defocusing event may actually cause an increase in energy if the receiver is located sufficiently off-axis; this situation being quite likely for Event 44. In the focusing condition, as two solitons surround the source, we see that the horizontal sound channel has little energy from mode 1, as it was not initially excited and is not easily trapped. However, the higher order modes are well-trapped by the soliton waveguide. Modes 3 and above begin to show secondary ducting in succeeding soliton waveguides, showing the influence of higher order modes in the depth integrated intensity plot.

B. Frequency dependence

Because we are using Eq. (3) to approximate the energy received from a broadband time arrival, based upon N frequencies, it is prudent to examine the frequency dependence of NIW

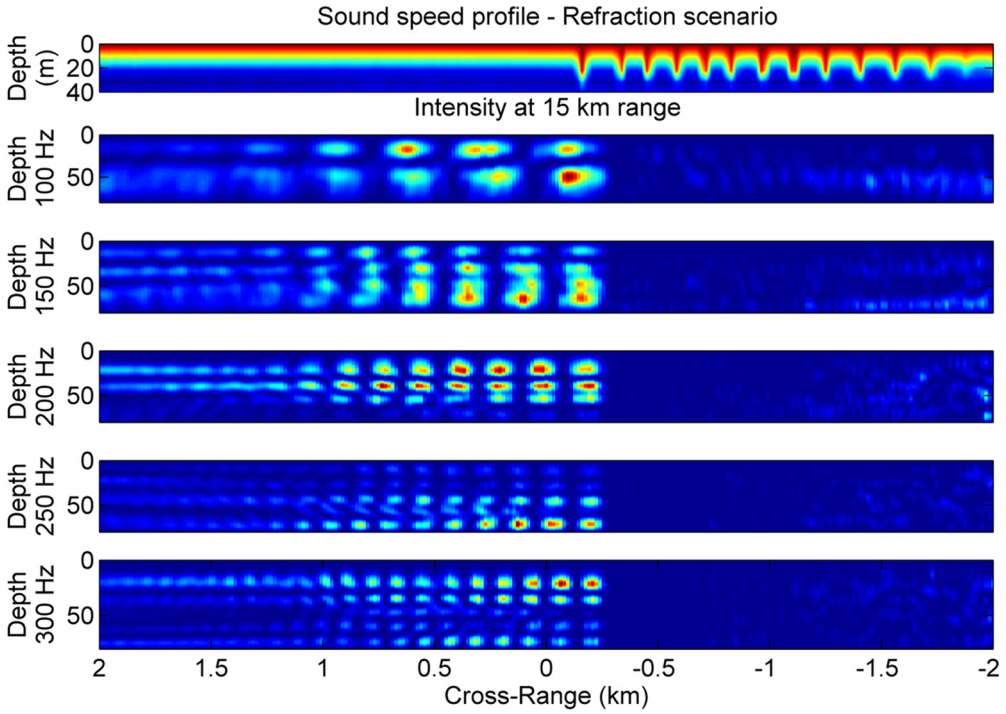

FIG. 7. (Color online) Frequency dependence during a refraction scenario. The sound speed input is valid across range (top). Normalized intensity at 15 km range for various frequencies (lower panels).

perturbations in the sound field. Figure 7 shows normalized intensity at 15 km range during a refraction scenario, indicating differences across the bandwidth are considerable. The Lloyd's mirror interference pattern in the cross-range (horizontal) dimension shows finer granularity at higher frequencies. Similarly, the depth dependence is more detailed at 300 Hz versus 100 Hz. The broadband energy metric, I_f, that we use condenses this frequency variability into a single measure. In our analysis we have normalized this metric such that the mean is one; $\langle I_f \rangle = 1$.

Figure 8 shows the frequency dependence for modes 1–5, compared to the broadband energy metric I_f, in a refraction scenario, and at 15 km range. Broadband energy is plotted immediately below the sound speed profile in two forms. When plotted versus depth, this can be interpreted as collapsing the plots shown in Fig. 7 into one. The "point" measurements plot uses a similar approach to our treatment of measured data and is well-suited for statistical analysis. In both plots, we see the effect of a horizontal refraction interference pattern as a series of peaks and nulls in energy versus cross-range in the unperturbed portion of the water column. Figure 8 also contains plots illustrating the frequency dependence of each mode. A curtained effect is immediately recognizable, where the horizontal interference pattern shows strong frequency dependence for each mode. The important point to be made here is that the broadband interference pattern shown in I_f is actually a combination of frequency-dependent and mode-dependent interference patterns.

C. Broadband time-dependent NIW propagation

To simulate Event 44 over space and time, roughly 4000 individual 3-D model runs were executed, which sampled the acoustic signal at 17 frequencies over the 100–300 Hz bandwidth, and propagated the NIW 10 km in 40-m marching increments. Consolidating the frequency bandwidth into the energy metric I_f reduces the problem to just over 200 marching steps, each with an energy profile at 15 km range. This yields a simulated time-varying "slice" of water column at 15 km range, which we employ in a statistical analysis.

Compiling all energy values for each water column slice provides a sample size of roughly 14×10^6 points. We have removed the absorbing boundary layers and the simulated ocean bottom in this sample set. This can also be interpreted as a very densely sampled rectangular array (60 000 elements) that is roughly 6 km wide and spans the entire 80-m water column. The center of this array would be 15 km away from the acoustic source, and each element records 200 measurements as they witness the NIW train pass by. It is our goal to break these data into regimes that show spatial dependence (i.e., the impact on angle between the NIW and acoustic track) and time dependence (i.e., NIW activity before versus during). Therefore, we require a reference value for both the mean and variance. We choose to use the mean and variance for the entire data set, which we have normalized such that the overall mean is unity; $\langle I_f \rangle = 1$.

Figure 4(d) shows a normalized histogram of the complete data set, which is best fit by a lognormal distribution. The purpose of fitting our entire data set is to create a reference point for breaking these data down further, and to choose the optimal approach for mean and variance calculations upon discrete portions of the data. The lognormal distribution for modeled intensity fluctuations has been previously argued by Tang *et al.*,[41] where a numerical Monte Carlo study using

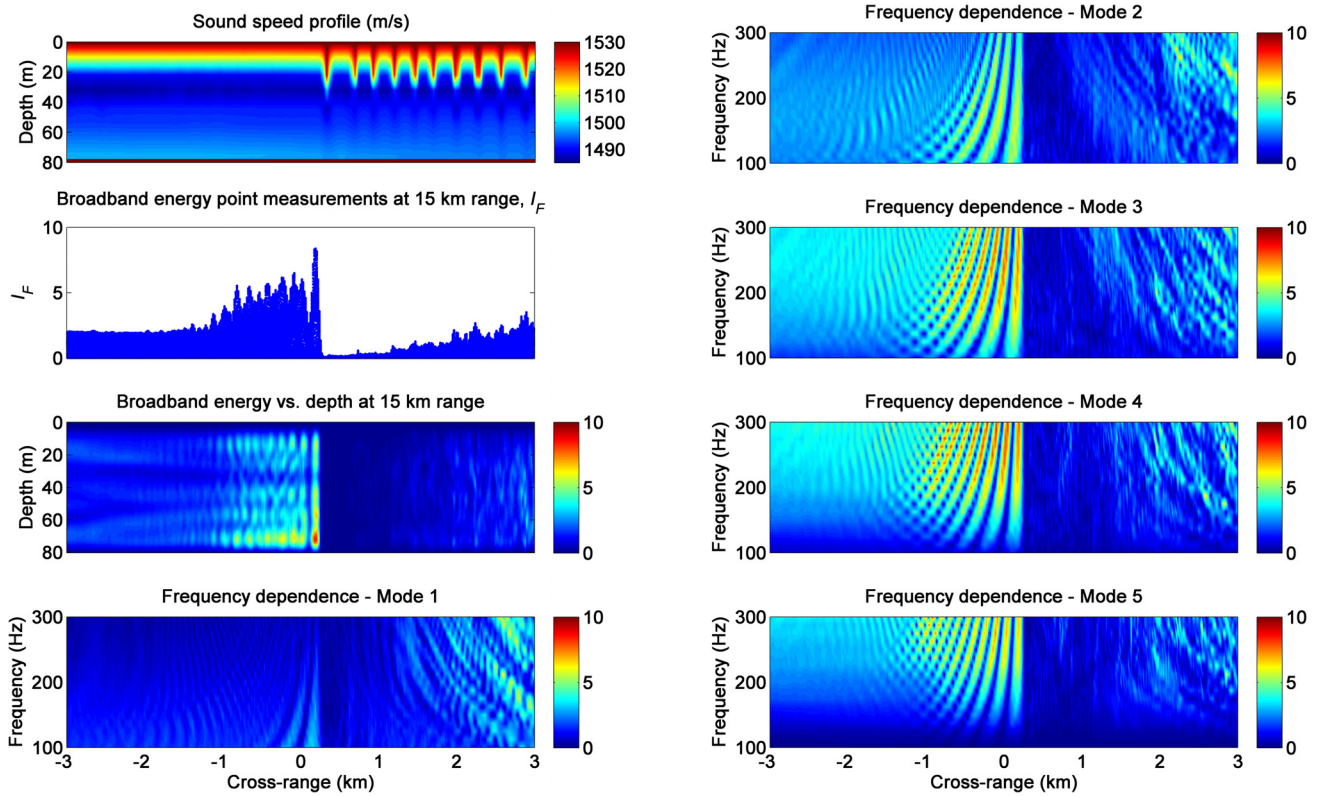

FIG. 8. (Color online) Broadband modal energy during a refraction condition is compared to modal decomposition of the PE field. Modal decomposition plots show mode amplitude at 15 km versus cross-range and frequency.

UMPE simulations examined intensity scintillations due to the linear internal wave spectra. These data as a whole are best fit by the lognormal distribution ($\hat{\mu} = 1.06$, $\hat{\sigma} = 1.36$), though certain subsets tend to an exponential distribution, warranting this calculation as a separate reference ($\hat{\mu} = 1.02$, $\hat{\sigma} = 1.04$).

D. Effects upon small angle variations

The first dissection of modeled data is upon the relative angle between the acoustic track and the propagating NIW, α. Recalling the original acoustic problem posed in Fig. 1, what will be the difference in received signals given different receiver locations? Suppose we have five receiving arrays at our disposal, and we position them at $\alpha = -4°, -2°, 0°, 2°, 4°$, where a negative bearing would correspond to the NIW arriving at the receiving array prior to the source. This scenario is depicted in Mm. 2 at 100 Hz. Figure 9 shows expected energy arrivals upon each array based upon repeated PE simulations. The five top-left panels show point measurements which simulate energy receptions over time, each plot representing a simulated array position. These data are *re*-normalized such that the mean energy in each panel is unity; $\langle I_{f,\alpha} \rangle = 1$. This is done so that we can more easily interpret results across a constant scale. In order to directly compare energy fluctuations at different angles, one can refer to the histograms shown on the right. Histogram data were *not* re-normalized and are direct subsets of data shown in Fig. 4(d). As a reference, the NIW sound speed profile is plotted below, and represents what the acoustic source is experiencing versus time. This profile is valid for the absolutely parallel case ($\alpha = 0°$) since it extends uniformly across range. However, it is not representative of what the other receiving VLAs experience, since they will observe a "shifted" version of the same profile. An asterisk is placed at the point where the first soliton reaches the VLA to help interpret this relative shift.

Mm. 2. The simulated internal wave traverses a 100 Hz sound field. Depth integrated intensity shows refraction, focusing, and defocusing effects. Simulated vertical line arrays are spaced in two degree increments at 15 km range. This is a file type of "mp4" (7.3 MB).

Let us examine the different angle scenarios. First, consider the condition when the NIW reaches the acoustic source before the receiver, corresponding to $\alpha = 4°, 2°$, shown in the uppermost panels of Fig. 9. We observe a steady ramping of energy prior to the NIW's arrival at either the source or receiver, peaking sharply just prior to the first soliton reaching the acoustic source. This sharp high-energy reception stems from a defocusing event at the source, vectoring energy 4 deg off-axis. This is followed by a quelled period of vacillating energy that corresponds to the duration of strongest NIW

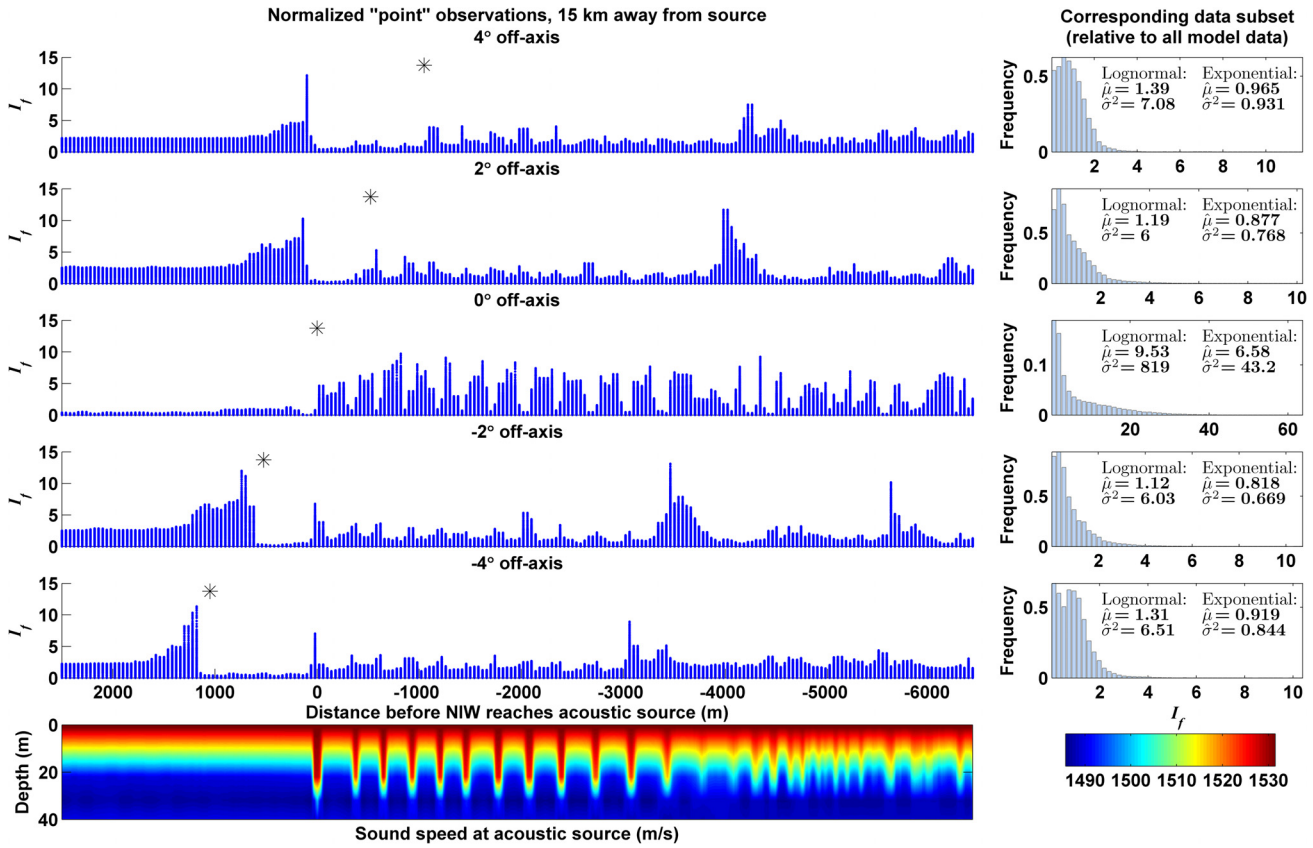

FIG. 9. (Color online) Energy dependence for instances where the acoustic track is nearly parallel to the NIW front. Acoustic angle is varied between ± 4° to show large variability of acoustic receptions for very small angle variations. Left-most panels simulate the NIW marching across distance (or time). These data re-normalized for each individual plot. Right-most panels show the associated distributions with the expected mean and variance annotated. Mean and variance values are referenced to the entire model data set. NIW sound speed at source provided as a reference. First soliton arrival at each receiving location marked by the asterisks.

activity. While one may expect the region of highest soliton activity to create the largest fluctuations, the receiver is located sufficiently off-axis and trapped energy is being completely vectored away from the array. Once the strongest solitons have passed, another brief period of energy arrives due to refraction by the strongest solitons. Following this, smaller perturbations towards the end of the NIW train continue to create smaller (but not insignificant) fluctuations. The histograms, mean, and variance for $\alpha = 4^\circ, 2^\circ$ indicate that energy delivery on these arrays is slightly higher than the overall sample set, and the fluctuations are more severe. Interestingly, more energy and increased variability is received at $\alpha = 4^\circ$ versus $\alpha = 2^\circ$, because the effects of defocusing are more prominent at this slightly wider angle.

Moving to the exactly parallel case, we notice a very different result for $\alpha = 0^\circ$. After re-normalizing these simulated receptions, we see that refraction prior to the NIW event is of secondary importance when compared to energy fluctuations received during soliton activity. Dramatic spikes and fades occur that align well with individual soliton arrivals. As the strongest solitons pass, the fluctuations become less periodic, but are still substantial. Compared to the previous cases when $\alpha = 4^\circ, 2^\circ$, the average energy upon the receiving VLA is about seven to nine times the sample-set's reference value. Further, the signal variability is an order of magnitude higher.

Examining the case for $\alpha = -4^\circ, -2^\circ$, we see strikingly similar patterns as $\alpha = 4^\circ, 2^\circ$. In this instance, the NIW reaches the receiving VLA prior to the acoustic source, similar to Event 44. Again, the ramping feature indicates horizontal refraction prior to the NIW event is an important effect. In each instance a period of suppressed energy exists immediately after the ramp. This is because the leading soliton creates a barrier, shielding energy from the receiver until it has completely crossed the entire acoustic track. Once the NIW has passed both the source and receiver, fluctuations begin to appear. As in $\alpha = 4^\circ, 2^\circ$, they are of smaller scale. For $\alpha = -2^\circ$, the backend refraction effect appears once more. Mean energy and variability is similar to the previous off-axis conditions.

An additional, and often used, measure of signal variability is the scintillation index, defined here as

$$SI_{(I_f)} = \frac{\langle I_f^2 \rangle}{\langle I_f \rangle^2} - 1. \tag{4}$$

Scintillation index is fundamentally a measure of signal variability, and is often associated with scattering, usually due to surface and bottom roughness. $SI > 1$ is also referred to as a limit for saturation,[42] where the pressure field is represented by an incoherent summation of random contributing wavefronts. Our concern is not with surface or bottom scattering, and therefore the PE model was not tailored to account for those factors. However, water-column inhomogeneity due to the NIW field, and energy transfer into the bottom, can cause severely distorted wavefronts and create large fluctuations in the acoustic field. In our case, for SI to breach unity, we require high intensity events to dominate a relatively low background energy. Scintillation index dependence for I_f is shown in Fig. 10 versus angle (or cross-range). We see that as the acoustic track draws closer to exactly parallel, SI increases. Inside the $\pm 1^\circ$ domain, SI is much greater than one, representing the sharply vacillating sound field the receiver experiences as repeated soliton waveguides pass the acoustic track.

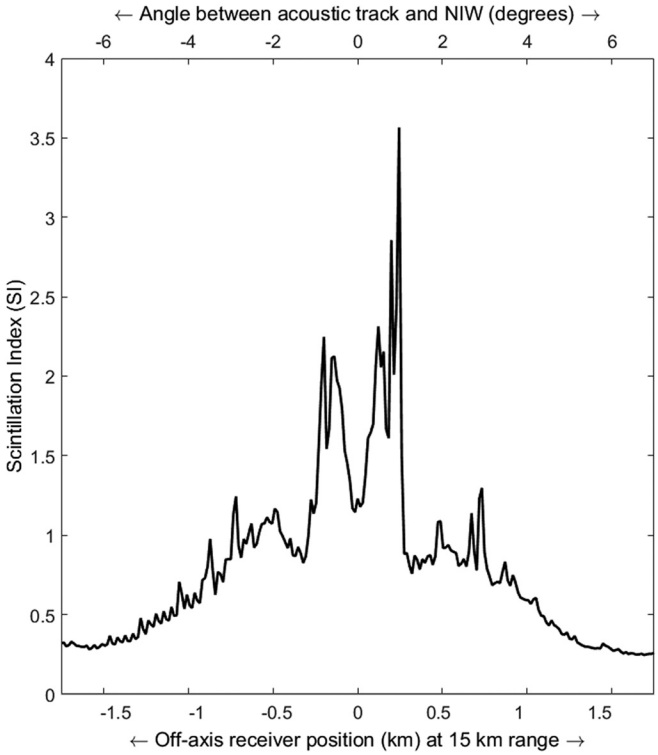

FIG. 10. Scintillation index of broadband energy compared to receiver position relative to the acoustic source (measured in degrees or kilometers).

E. Time-varying fluctuation regimes

Similar to our treatment of measured data, in order to compare the importance of refraction *prior* to the NIW's arrival relative to fluctuations *during* NIW activity, we can delineate the simulated time arrivals into time-varying fluctuation regimes. We define the time before the NIW reaches the source–receiver path as the *refraction regime*, and the time after the NIW has crossed the entire acoustic track as the *NIW interference regime*. Table II compares the mean energy arrivals at a virtual receiving array for $\alpha = -4^\circ, -2^\circ, 0^\circ, 2^\circ, 4^\circ$; the values are calculated from subsets of the entire modeled data set.

When the NIW is perfectly parallel to the source–receiver track, the receiver will observe intense signal amplifications due to refraction and focusing effects. In this case, the horizontal Lloyd's mirror and focusing between solitons provides

TABLE II. Simulated mean energy arrival at virtual receiver.

Angle difference, α (S-R track vs NIW front)	Refraction regime	NIW interference regime
-4°	$\mu = 1.771$	$\mu = 1.225$
-2°	$\mu = 1.953$	$\mu = 0.8798$
0°	$\mu = 2.356$	$\mu = 12.55$
$+2^\circ$	$\mu = 2.08$	$\mu = 0.8828$
$+4^\circ$	$\mu = 1.864$	$\mu = 1.275$

maximum impact. However, when the receiver is not perfectly parallel, refraction prior to the NIW's arrival causes more signal amplification than when the NIW crosses the source–receiver track. This latter situation is the condition we witnessed aboard the R/V Sharp during Event 44.

V. SUMMARY AND CONCLUSIONS

In summary, measured data from the SW06 experiment exhibit general features that can be characterized by a time-varying scenario where the acoustic track is nearly parallel to an approaching NIW train. Further insight into the measured data is offered through the use of broadband energy metrics, modal decomposition, and statistical analysis. A breakdown of measured data based upon time-varying regimes is offered. To better interpret the observational data, we have implemented the MMPE algorithm to closely examine shallow water propagation when nonlinear internal waves dominate the sound field. We first examined a narrowband scenario to illustrate how the mechanisms of refraction, defocusing, and focusing induce fluctuations in the sound field. Finally, we simulated a propagating NIW traversing through a broadband acoustic field and used a statistical approach to (1) infer spatial differences by varying the acoustic track angle, and (2) temporal differences based upon time-varying fluctuation regimes.

To conclude, 3-D PE modeling has served as a highly informative tool to better-understand the complex problem of acoustic propagation in the presence of NIWs. The primary benefit of our modeling approach is that we have removed the constraint of an undersampled ocean—which exists in the measured field data. One could build upon this study by adding additional environmental perturbations to the model such as NIW curvature or bathymetry variations. Our work is complementary to many other efforts in this area of study, and we expand it by further elaborating upon azimuthal dependencies that fall within the horizontal refraction and focusing regimes. In this situation, the difference between an acoustic track *exactly parallel* to a propagating NIW front versus being *slightly askew* is significant. In perfectly ideal conditions, during the exactly parallel case, focusing becomes a first order factor, and refraction prior to the NIW's arrival has secondary influence. We are *not* suggesting refraction prior to the NIW's arrival is unimportant—in fact, a slightly off-axis configuration will result in refraction effects that are similar to fluctuations during NIW activity, if not greater. Further, because the ideal circumstances are potentially less likely in real-world scenarios, refraction effects may be more commonplace in the shallow water environment.

ACKNOWLEDGMENTS

This work would have not been possible without support from the Office of Naval Research, specifically Ben Reeder. We extend additional thanks to the hardworking individuals who supported the SW06 experiment, which served as the motivation for this work. This work benefited from rich technical discussions with Jim Lynch, Ying Tsong Lin, and Art Newhall (WHOI) and Steven Crocker (URI). This work would not have been possible without the help and resources from the University of Rhode Island Engineering and Computer Center.

[1]A. E. Newhall, T. F. Duda, K. Von Der Heydt, J. D. Irish, J. N. Kemp, S. A. Lerner, S. P. Liberatore, Y. T. Lin, J. F. Lynch, A. R. Maffei, A. K. Morozov, A. A. Shmelev, C. J. Sellers, and W. E. Witzell, "Acoustic and oceanographic observations and configuration information for the WHOI moorings from the SW06 experiment," WHOI technical report No. WHOI-2007-04 (2007), available at https://hdl.handle.net/1912/1826.

[2]J.-x. Zhou, X.-z. Zhang, and P. H. Rogers, "Resonant interaction of sound wave with internal solitons in the coastal zone," J. Acoust. Soc. Am. **90**(4), 2042–2054 (1991).

[3]B. G. Katsnelson and S. A. Pereselkov, "Low-frequency horizontal acoustic refraction caused by internal wave solitons in a shallow sea," Acoust. Phys. **46**(6), 684–691 (2000).

[4]S. Finette and R. Oba, "Horizontal array beamforming in an azimuthally anisotropic internal wave field," J. Acoust. Soc. Am. **114**(1), 131–144 (2003).

[5]M. Badiey, B. G. Katsnelson, J. F. Lynch, S. Pereselkov, and W. L. Siegmann, "Measurement and modeling of three-dimensional sound intensity variations due to shallow-water internal waves," J. Acoust. Soc. Am. **117**(2), 613–625 (2005).

[6]M. Badiey, Y. Mu, J. Lynch, J. Apel, and S. Wolf, "Temporal and azimuthal dependence of sound propagation in shallow water with internal waves," IEEE J. Ocean. Eng. **27**(1), 117–129 (2002).

[7]T. F. Duda, "Examining the validity of approximations to fully three-dimensional shallow-water acoustic propagation through nonlinear internal gravity waves," in *OCEANS 2007-Europe*, pp. 1–5 (2007).

[8]S. Finette, M. H. Orr, A. Turgut, J. R. Apel, M. Badiey, C.-s. Chiu, R. H. Headrick, J. N. Kemp, J. F. Lynch, A. E. Newhall, K. v. Heydt, B. Pasewark, S. N. Wolf, and D. Tielbuerger, "Acoustic field variability induced by time evolving internal wave fields," J. Acoust. Soc. Am. **108**(3), 957–972 (2000).

[9]S. D. Frank, M. Badiey, J. F. Lynch, and W. L. Siegmann, "Analysis and modeling of broadband airgun data influenced by nonlinear internal waves," J. Acoust. Soc. Am. **116**(6), 3404–3422 (2004).

[10]S. D. Frank, M. Badiey, J. F. Lynch, and W. L. Siegmann, "Experimental evidence of three-dimensional acoustic propagation caused by nonlinear internal waves," J. Acoust. Soc. Am. **118**(2), 723–734 (2005).

[11]R. Oba and S. Finette, "Acoustic propagation through anisotropic internal wave fields: Transmission loss, cross-range coherence, and horizontal refraction," J. Acoust. Soc. Am. **111**(2), 769–784 (2002).

[12]M. Badiey, B. G. Katsnelson, Y. T. Lin, and J. F. Lynch, "Acoustic multipath arrivals in the horizontal plane due to approaching nonlinear internal waves," J. Acoust. Soc. Am. **129**(4), EL141–EL147 (2011).

[13]Y.-T. Lin, T. F. Duda, and J. F. Lynch, "Acoustic mode radiation from the termination of a truncated nonlinear internal gravity wave duct in a shallow ocean area," J. Acoust. Soc. Am. **126**(4), 1752–1765 (2009).

[14]J. F. Lynch, Y. T. Lin, T. F. Duda, and A. E. Newhall, "Acoustic ducting, reflection, refraction, and dispersion by curved nonlinear internal waves in shallow water," IEEE J. Ocean. Eng. **35**(1), 12–27 (2010).

[15]K. G. McMahon, L. K. Reilly-Raska, W. L. Siegmann, J. F. Lynch, and T. F. Duda, "Horizontal Lloyd mirror patterns from straight and curved nonlinear internal waves," J. Acoust. Soc. Am. **131**(2), 1689–1700 (2012).

[16]Y. T. Lin, K. G. McMahon, J. F. Lynch, and W. L. Siegmann, "Horizontal ducting of sound by curved nonlinear internal gravity waves in the continental shelf areas," J. Acoust. Soc. Am. **133**(1), 37–49 (2013).

[17]B. J. Sperry, J. F. Lynch, G. Gawarkiewicz, C.-S. Chiu, and A. Newhall, "Characteristics of acoustic propagation to the eastern vertical line array receiver during the summer 1996 New England shelfbreak PRIMER experiment," IEEE J. Ocean. Eng. **28**(4), 729–749 (2003).

[18]J. R. Apel, M. Badiey, C.-S. Chiu, S. Finette, R. Headrick, J. Kemp, J. F. Lynch, A. Newhall, M. H. Orr, B. H. Pasewark, D. Tielbuerger, A. Turgut, K. Von Der Heydt, and S. Wolf, "An overview of the 1995 SWARM shallow-water internal wave acoustic scattering experiment," IEEE J. Ocean. Eng. **22**(3), 465–500 (1997).

[19]R. H. Headrick, J. F. Lynch, J. N. Kemp, A. E. Newhall, K. von der Heydt, J. Apel, M. Badiey, C.-S. Chiu, S. Finette, M. Orr, B. Pasewark, A. Turgot, S. Wolf, and D. Tielbuerger, "Acoustic normal mode fluctuation statistics in the 1995 SWARM internal wave scattering experiment," J. Acoust. Soc. Am. **107**, 201–220 (2000).

[20]J. F. Lynch, S. R. Ramp, C.-S. Chiu, T. Y. Tang, Y. J. Yang, and J. A. Simmen, "Research highlights from the Asian Seas International Acoustics Experiment in the South China Sea," IEEE J. Ocean. Eng. **29**(4), 1067–1074 (2004).
[21]P. H. Dahl, R. Zhang, J. H. Miller, L. R. Bartek, Z. Peng, S. R. Ramp, J. X. Zhou, C. S. Chiu, J. F. Lynch, J. A. Simmen, and R. C. Spindel, "Overview of results from the Asian seas international acoustics experiment in the east china sea," IEEE J. Ocean. Eng. **29**(4), 920–928 (2005).
[22]M. Badiey, B. G. Katsnelson, J. F. Lynch, and S. Pereselkov, "Frequency dependence and intensity fluctuations due to shallow water internal waves," J. Acoust. Soc. Am. **122**(2), 747–760 (2007).
[23]J. Luo, M. Badiey, E. A. Karjadi, B. Katsnelson, A. Tskhoidze, J. F. Lynch, and J. N. Moum, "Observation of sound focusing and defocusing due to propagating nonlinear internal waves," J. Acoust. Soc. Am. **124**(3), 66 (2008).
[24]J. F. Lynch, J. A. Colosi, G. G. Gawarkiewicz, T. F. Duda, A. D. Pierce, M. Badiey, B. G. Katsnelson, J. E. Miller, W. Siegmann, C.-S. Chiu, and A. Newhall, "Consideration of fine-scale coastal oceanography and 3-D acoustics effects for the ESME sound exposure model," IEEE J. Ocean. Eng. **31**(1), 33–48 (2006).
[25]K. B. Smith and J. A. Colosi, "Effects of solitons on acoustic energy flow in three dimensions," J. Acoust Soc. Am. **132**, 3942 (2008).
[26]T. F. Duda, J. F. Lynch, A. E. Newhall, L. Wu, and C.-S. Chiu, "Fluctuation of 400-Hz sound intensity in the 2001 ASIAEX South China Sea experiment," IEEE J. Ocean. Eng. **29**(4), 1264–1279 (2004).
[27]A. Fredricks, J. A. Colosi, J. F. Lynch, G. Gawarkiewicz, C.-S. Chiu, and P. Abbot, "Analysis of multipath scintillations from long range acoustic transmissions on the New England continental slope and shelf," J. Acoust. Soc. Am. **117**(3), 1038–1057 (2005).
[28]S. E. Crocker, J. H. Miller, G. R. Potty, and J. F. Lynch, "Nonlinear optimization for beamforming a geometrically deficient vertical line array: Application to sediment tomography," J. Acoust. Soc. Am. **120**(5), 3063–3063 (2006).
[29]K. B. Smith, "Convergence, stability, and variability of shallow water acoustic predictions using a split-step Fourier parabolic equation model," J. Comput. Acoust. **9**(1), 243 (2001).
[30]K. B. Smith and F. D. Tappert, "Horizontal refraction and the uncoupled azimuth approximation," Theor. Comput. Acoust. **2003**, 343–354 (2004).
[31]D. J. Thomson and C. S. Bohun, "A wide-angle initial field for the parabolic equation models," J. Acoust. Soc. Am **83**, S118 (1988).
[32]Y.-M. Jiang, N. R. Chapman, and M. Badiey, "Quantifying the uncertainty of geoacoustic parameter estimates for the New Jersey shelf by inverting air gun data," J. Acoust. Soc. Am. **121**(4), 1879–1894 (2007).
[33]G. R. Potty, J. H. Miller, P. S. Wilson, J. F. Lynch, and A. Newhall, "Geoacoustic inversion using combustive sound source signals," J. Acoust. Soc. Am. **124**(3), E146 (2008).
[34]Z. Y. Zhang and C. T. Tindle, "Improved equivalent fluid approximations for a low shear speed ocean bottom," J. Acoust. Soc. Am. **98**(6), 3391–3396 (1995).
[35]M. B. Porter, "The KRAKEN normal mode program," Technical report, SACLANT Undersea Research Center (1992).
[36]R. H. Ferris, "Comparison of measured and calculated normal-mode amplitude functions for acoustic waves in shallow water," J. Acoust. Soc. Am. **52**(3B), 981–989 (1972).
[37]A. R. Smith and K. B. Smith, "Mode functions for the wide-angle approximation to the parabolic equation," J. Acoust. Soc. Am. **103**(2), 814–821 (1998).
[38]G. A. Dossot, "Acoustic fluctuations in shallow water due to nonlinear internal waves," Ph.D. dissertation, Ocean Engineering, University of Rhode Island, 2011.
[39]J. A. Colosi, "Acoustic mode coupling induced by shallow water nonlinear internal waves: Sensitivity to environmental conditions and space–time scales of internal waves," J. Acoust. Soc. Am. **124**(3), 1452–1464 (2008).
[40]T. F. Duda, "Acoustic mode coupling by nonlinear internal wave packets in a shelfbreak front area," IEEE J. Ocean. Eng. **29**(1), 118–125 (2004).
[41]X. Tang, F. D. Tappert, and D. B. Creamer, "Simulations of large acoustic scintillations in the Straits of Florida," J. Acoust. Soc. Am. **120**(6), 3539–3552 (2006).
[42]J. A. Colosi and A. B. Baggeroer, "On the kinematics of broadband multipath scintillation and the approach to saturation," J. Acoust. Soc. Am. **116**(6), 3515–3522 (2004).